



Probing joint strength and distortion in gas metal arc lap joining of aluminum and steel sheets

Sven-F Goecke¹ · P. Makwana² · M. Shome³ · A. De²

Received: 11 September 2017 / Accepted: 14 September 2018 / Published online: 24 October 2018
© International Institute of Welding 2018

Abstract

Joining of multi-metallic assemblies such as aluminum and steel sheets using fusion joining technologies is prudent although the formation of intermetallic compounds along joint interface has remained a critical challenge. An advanced, low-power input, gas metal arc process was employed here for joining of aluminum and zinc-coated steel sheets of dissimilar thicknesses in lap-joint configuration. The heat input during the process was restricted by fast responsive current and voltage pulses that allowed a synchronized arcing and short circuiting at a low arc power. The effect of heat input and thermophysical properties of base materials on the bead profile, joint strength, and distortion was studied extensively. The results indicated a rational improvement of joint quality with lowering of the heat input within a restrictive range of processing conditions such as wire feed rate and travel speed. Most importantly, the mixed-metal assembly exhibited different thermal distortions with the aluminum top sheet undergoing greater distortion than the bottom steel sheet due to a higher coefficient of thermal expansion.

Keywords Gas metal arc joining · Mixed-metal assembly · Aluminum alloy · Zinc-coated steel · Thermal distortion

1 Introduction

Mixed-metal assemblies such as aluminum and zinc-coated steel sheets are increasingly considered a potential route to reduce overall weights of vehicular and structural parts. However, joining of such mixed-metal assemblies especially by fusion-joining processes has remained a major concern. In particular, the formations of brittle intermetallic compounds (IMC) at the joint interface and thermal distortion remain as prominent challenges [1]. Recent gas metal arc (GMA)-based advanced processes with responsive current and voltage pulses provide an opportunity to reduce the overall heat input and restrict thermal distortion and intermetallic compounds at the joint interface [2, 3]. A systematic study is therefore undertaken to examine the effectiveness of an

advanced gas metal arc-based joining process to reduce joint distortion and to improve joint quality in joining of aluminum and zinc-coated steel sheets.

A wide range of heat input and resulting joint strengths are reported as different fusion-based processes are used to join aluminum alloys and zinc-coated steel sheets. Zhang et al. recommended a heat input of around 61 J mm^{-1} and reported a corresponding peak joint strength of 96 MPa in GMA-based joining of AA6061 to zinc-coated Q235 steel sheets using a 1.0-mm-diameter AA4043 filler wire [4]. Su et al. suggested an optimum heat input of 85 J mm^{-1} in joining of AA5052 and zinc-coated steel sheets using a 1.2-mm-diameter AA4047 filler wire [5]. These authors reported a bead width of around 4.4 mm and peak joint strength of 200 MPa [5]. In contrast, Cao et al. recorded a similar bead width and joint strength at a much higher heat input of 200 J mm^{-1} in joining of AA6061 and zinc-coated Q235 steel sheets using a AA4047 filler wire [6]. The sheet thicknesses were limited from 1.0 to 1.2 mm in all these studies. The above studies indicate a general lacuna in quantitative understanding of the effect of heat input on bead profile and the joint strength in joining of aluminum alloys and zinc-coated steel sheets.

The formation of Fe-Al IMCs along the joint interface and their growth showed significant influence on the final strength and location of failure in joints of aluminum and steel sheets.

Recommended for publication by Commission XII - Arc Welding Processes and Production Systems

✉ Sven-F Goecke
goecke@th-brandenburg.de

¹ Technical University of Applied Science, Brandenburg an der Havel, Germany

² Indian Institute of Technology, Bombay, India

³ Tata Steel Ltd., Jamshedpur, India

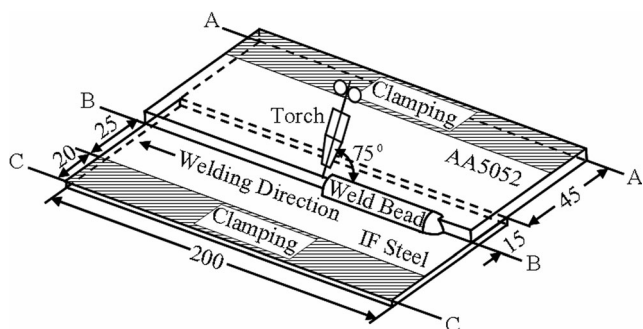


Fig. 1 Schematic setup of aluminum alloy and galvanized steel sheet assembly in lap-joint configuration

Dong et al. reported an interface phase layer thickness of $6.0\ \mu\text{m}$ and peak joint strength of $134\ \text{MPa}$ corresponding to a heat input of $145\ \text{J mm}^{-1}$ in joints of AA5A02 and Q235 steel [7]. Yang et al. observed a phase layer thickness of $5.0\ \mu\text{m}$ corresponding to the peak joint strength of $146\ \text{MPa}$ at a heat input of $122\ \text{J mm}^{-1}$ in joints of AA6061 and zinc-coated steel sheets [8]. A permissible range of interface phase layer thicknesses from 2.9 to $4.0\ \mu\text{m}$ with the peak joint strength of around $160\ \text{MPa}$ was reported by Yagati et al. in dissimilar joints of aluminum alloys and zinc-coated sheets corresponding to a heat input ranges of 48 to $70\ \text{J mm}^{-1}$ [9]. Das et al. used a heat input range of 110 to $156\ \text{J mm}^{-1}$ and reported the interface phase layer thicknesses of around 4.3 to $5.0\ \mu\text{m}$ with the peak joint strength as $140\ \text{MPa}$ in joints of AA5052 and zinc-coated steel sheets [10]. Most of these studies reported failures along the joint interface and attributed the same to the presence of brittle Fe–Al IMCs although occasional failures through the aluminum top sheet was also noted especially at lower heat inputs.

Thermal distortion has always remained another major concern when joining of thin metallic sheets in comparison to the thicker plates due to the lower flexural rigidity of thinner sheets [11]. Goecke et al. reported a 27% reduction of thermal distortion by shifting from a standard pulsed current GMA to a short-circuiting GMA process for welding of 1.6 mm high-strength steels [12]. The authors attributed the reduction in joint distortion to decrease in overall heat input [12]. Frostevarg et al. reported a 35% decrease in joint distortion in GMA welding of 3.0-mm steel sheets when the heat input was reduced from 230 to $145\ \text{J mm}^{-1}$ [13]. Schenk et al. reported a 33% drop in thermal distortion in GMA welding of 1.0-mm-thick steel sheets when the joint restraint was removed after the assembly reached ambient temperature as opposed to immediate release of the assembly

on conclusion of joining [14]. The nature of thermal distortion in joining of dissimilar alloys such as aluminum and zinc-coated steel is complex in nature due to different thermophysical properties of the metallic sheets and studies in this direction are scarce in published literature.

A systematic investigation on joining of aluminum and zinc-coated steel sheets is therefore undertaken in the present work using an advanced GMA-based process that allows high-resolution control of current and voltage pulses to restrict the overall arc power. The effect of heat input on the bead profile, peak joint strength, and the nature of variations in joint distortion are studied in detail. An optimum range of process conditions and corresponding heat inputs is recommended to reduce the overall joint distortion and restrict the growth of the interface layer with Fe–Al IMC along the joint interface.

2 Experimental investigation

Hot-dipped galvanized interstitial free (GI-IF) steel sheets of 0.8 mm thickness were joined to 1.0-mm-thick AA5052 alloy sheets in a lap joint geometry (Fig. 1) using a 1.0-mm-diameter filler wire of AA4043 alloy. Table 1 lists the chemical composition of the sheets and the filler wire. An advanced pulsed current GMA power source was used in a typical short-circuiting mode of metal transfer for all the joining experiments. Pure argon (99.999%) was used as the shielding gas and employed at a flow rate of $15\ \text{L min}^{-1}$. The GMA torch was fixed at an angle of 75° in the direction of joint line with the filler wire tracing along the edge of the top sheet (Fig. 1). A constant gap of 15 mm was maintained between the contact tip and sheet. The assembly of the sheets was restrained during joining as shown by a hatched section in Fig. 1.

The real-time current and voltage transients were recorded at a simultaneous sampling rate of 100 kHz using a four-channel pc-interfaced data logger. Table 2 shows the process conditions that were identified through exhaustive trials to obtain consistent bead profiles. The thermal distortion of the joint assembly was evaluated on a Zeiss Eclipse 700 bridge-type coordinate measuring machine (CMM) with a resolution of $0.5\ \mu\text{m}$. The extent of spread of the deposited filler alloy on the unmolten steel surface, which was referred to as the wetting length, and the existence of porosity on the bead deposit were inspected under optical microscope after polishing and etching of joint coupons with Keller's reagent. The interface layer thickness

Table 1 Chemical content (in wt%) and UTS (MPa) of metallic sheets and filler wire

	C	Fe	Zn	Mn	Mg	Si	Cu	P	S	Cr	Ti	Al	UTS
IF steel	0.002	Bal.	–	0.09	–	0.004	0.006	0.02	0.007	0.02	0.04	0.05	316
AA5052	–	0.4	0.1	0.1	2.5	0.25	0.1	–	–	0.15	0.15	Bal.	220
AA4043	–	0.8	0.1	0.05	0.05	5	0.3	–	–	–	0.2	Bal.	200

Table 2 Process conditions considered in current study

Wire feed rate (m min ⁻¹)	Joining speed (mm s ⁻¹)	I_{AV} (A)	V_{AV} (V)	Heat input (J mm ⁻¹)
4.0	5.0	45.9	11.4	84
4.5	7.5	50.8	11.6	63
5.0	5.0, 7.5, 10.0, 12.5	56.3	12.0	107, 71, 54, 40
5.5	7.5	62.0	12.2	81
6.0	7.5	66.9	12.6	90

was measured on the backscattered images taken on a FEI quanta 200 scanning electron microscope (SEM). The joint failure strength was evaluated in an Instron-3369 dual column universal testing system at a crosshead speed of 1 mm min⁻¹ and the samples were prepared following BS EN 12797:2000, 2004 [15]. Three specimens were tested to estimate the average failure strength for each condition.

3 Results and discussions

3.1 Estimation of heat input

Figure 2a, b shows the recorded current and voltage transients for a travel speed of 7.5 mm s⁻¹ at two different wire feed rates of 4.5 m min⁻¹ and 6.0 m min⁻¹. The short-circuiting period starts at the instant when there is a rapid drop in voltage to around 4 V and a sharp increase in current as seen in Fig. 2a, b that aids in pinching and deposition of the molten filler. The short-circuiting current is then reduced to commence the arcing stage at a low power reducing the overall heat input. An intense current pulse is subsequently applied which initiates the electrode tip melting followed by a steady drop in current till the beginning of the next short-circuiting phase. A comparison of Fig. 2a, b shows that the maximum current in the short-circuiting phase reduces from 150 A (± 7.3) to 130 A (± 3.2) while it remains constant at around 155 A (± 8.4) in the arcing stage with increase in the wire feed rate from 4.5 to 6.0 m min⁻¹. The values within the parenthesis indicate the deviation in measurements about the mean value. Figure 2a, b

also indicates an increase in the current pulse frequency as the wire feed rate is increased from 4.5 to 6.0 m min⁻¹ implying a higher melting rate of filler wire for process stability.

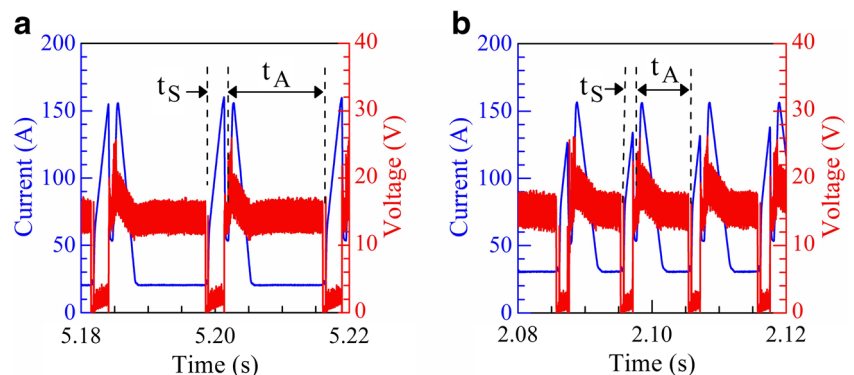
The time-averaged current (I_{AV}), voltage (V_{AV}), and arc power (P_{AV}) were estimated from the recorded current and voltage signals as:

$$I_{AV} = \frac{\sum_{i=0}^{\tau} I_i t_i}{\sum_{i=0}^{\tau} t_i} \quad V_{AV} = \frac{\sum_{i=0}^{\tau} V_i t_i}{\sum_{i=0}^{\tau} t_i} \quad P_{AV} = \frac{\sum_{i=0}^{\tau} I_i V_i t_i}{\sum_{i=0}^{\tau} t_i} \quad (1)$$

The variables t_i , I_i , and V_i refer to instantaneous values of time, current, and voltage respectively, and τ is either arcing (t_A) or short-circuiting (t_S) period. The time-averaged values of I_{AV} , V_{AV} , and P_{AV} were evaluated over twenty current pulses for each process condition. The linear heat input (q) was calculated as $q = (\eta P_{AV})/v$ for a travel speed (v), with the process efficiency η assumed as 0.8 [16]. Table 2 shows the time-averaged values of I_{AV} , V_{AV} , and the corresponding estimated values of heat input (q) for the range of process conditions considered here.

Figure 3a–c presents the variation in the time-averaged values of current, time durations, pulse frequency, and power for the short-circuiting and arcing periods as the wire feed rate is increased from 4.0 to 6.0 m min⁻¹. Figure 3a shows that the short-circuiting and arcing currents rise respectively from 63 A (± 2.6) to 73 A (± 3.7) and from 34 A (± 2.4) to 62 A (± 2.5) with increase in wire feed rate. In contrast, the time durations for the arcing period reduce from 13.35 ms (± 0.93) to 7.66 ms (± 0.69) and the short-circuiting duration remains nearly the same at 4.07 ms (± 0.59) as the wire feed rate is raised from 4.0 to

Fig. 2 Measured voltage and current transients for joining speeds of 7.5 mm s⁻¹ and wire feed rates of **a** 4.5 and **b** 6.0 m min⁻¹



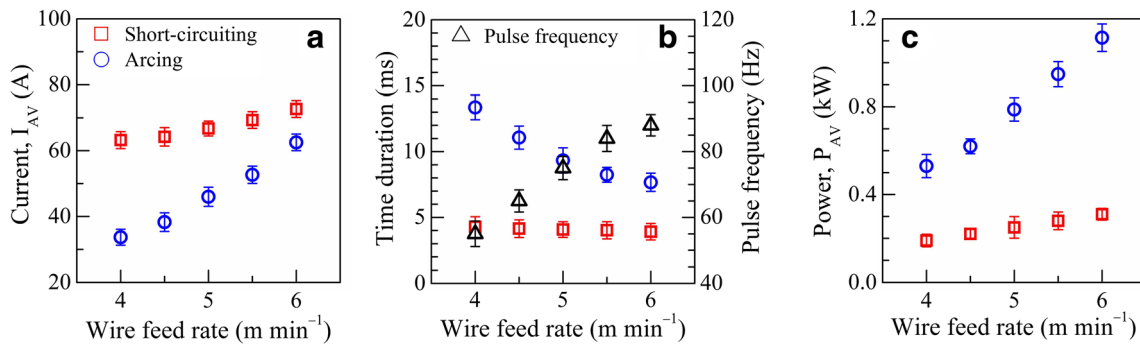


Fig. 3 Time-averaged values of short-circuiting and arcing **a** currents, **b** time durations and overall pulse frequency, and **c** powers as function of wire feed rate

6.0 m min⁻¹. Consequently, the current pulse frequency increases from 55 Hz (± 3.9) to 88 Hz (± 3.3) as seen in Fig. 3b. The arc powers during the short-circuiting and arcing periods are also increased from 0.19 kW (± 0.02) to 0.31 kW (± 0.03) and from 0.53 kW (± 0.05) to 1.11 kW (± 0.06), respectively, with rise in wire feed rate (Fig. 3c). A comparison of Figs. 2 and 3 depicts a significant influence of the transient nature of current and voltage on the arc power, and that a fast responsive regulation of current and voltage transient can reduce both the arc power and overall heat input.

3.2 Effect of heat input on bead profile

Figure 4a–c presents the cross-sectional macrographs of the deposited beads at three different heat inputs of 40 J mm⁻¹, 84 J mm⁻¹, and 107 J mm⁻¹, respectively. Since the top AA5052 sheet melts under the arc, the original unmelted geometry of the top sheet is indicated by a dotted line on the macrograph. It is noteworthy that the joint coupons have been sectioned at multiple locations along the deposit length for each processing condition to examine porosities, mechanical strength, and interface characteristics. Figure 4a–c presents the cross-sectional macrographs that have been devoid of

porosities for better readability of wetting length and contact angle. The representative sections with porosities at different heat inputs are presented in the subsequent section.

A comparison of Fig. 4a–c further shows the variation of the wetting length (R) of the filler alloy deposit on the unmelted bottom steel as function of heat input. For example, the wetting length (R) increased from 2.35 mm (± 0.20) to 4.55 mm (± 0.19) as the heat input was increased from 40 to 84 J mm⁻¹, and, to 4.77 mm (± 0.16) at the maximum heat input of 107 J mm⁻¹. Similarly, the toe angle (θ) of the bead profile reduces from 48° to 32° as the heat input is raised from 40 to 84 J mm⁻¹, and to 28° at the highest heat input of 107 J mm⁻¹. The acute bead toe angles indicate an improved wetting of the bottom steel sheet for the range of process conditions considered here [17].

Figure 4s shows the measured wetting lengths (R) and the contact angles (θ) at the toe point of the joint bead as a function of heat input for all the joint samples. With initial increase in heat input, the wetting length increases and the contact angle reduces consistently. The contact angle becomes nearly steady beyond a certain value ($\sim 28^\circ$) which corresponds to the equilibrium contact angle between aluminum and zinc [2]. The wetting length of the bead profile also ceases to increase

Fig. 4 Measured joint bead profiles as a function of heat inputs (in J mm⁻¹) of **a** 40, **b** 84, and **c** 107. **(d)** Variations in wetting length and contact angle of the filler wire deposit on the unmelted steel surface as a function of heat input

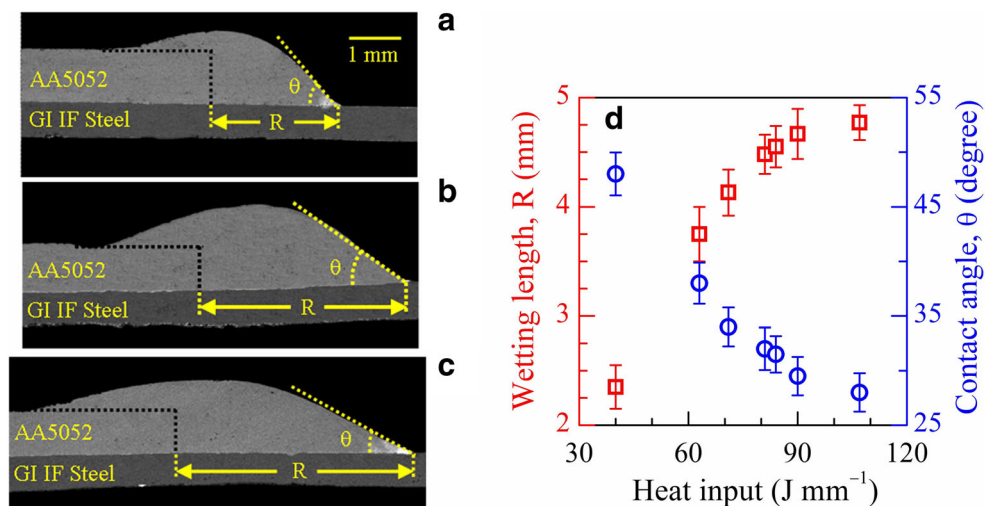
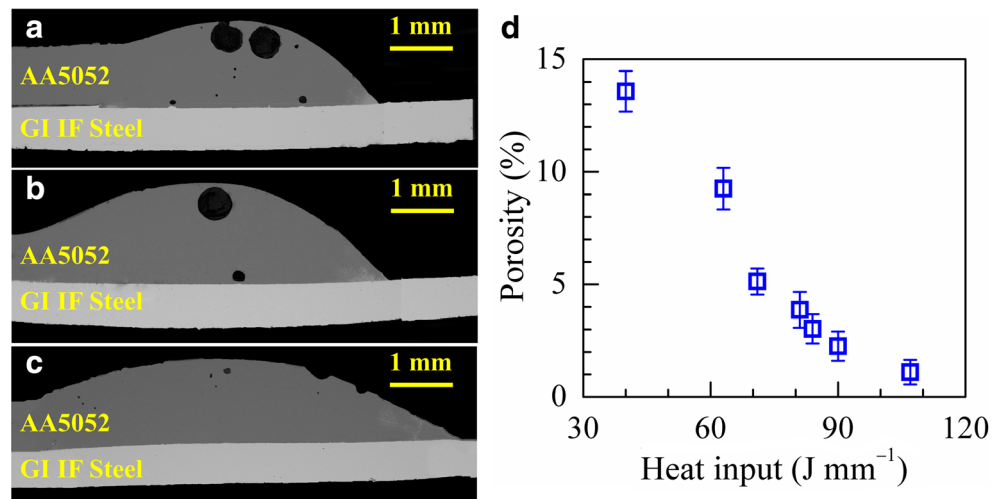


Fig. 5 Representative bead profiles showing porosity at three different heat inputs (in J mm^{-1}) of **a** 40, **b** 84, and **c** 107. **d** Variation in average bead porosity as a function of heat input



beyond 4.8 mm with further increase in heat input from 90 to 107 J mm^{-1} .

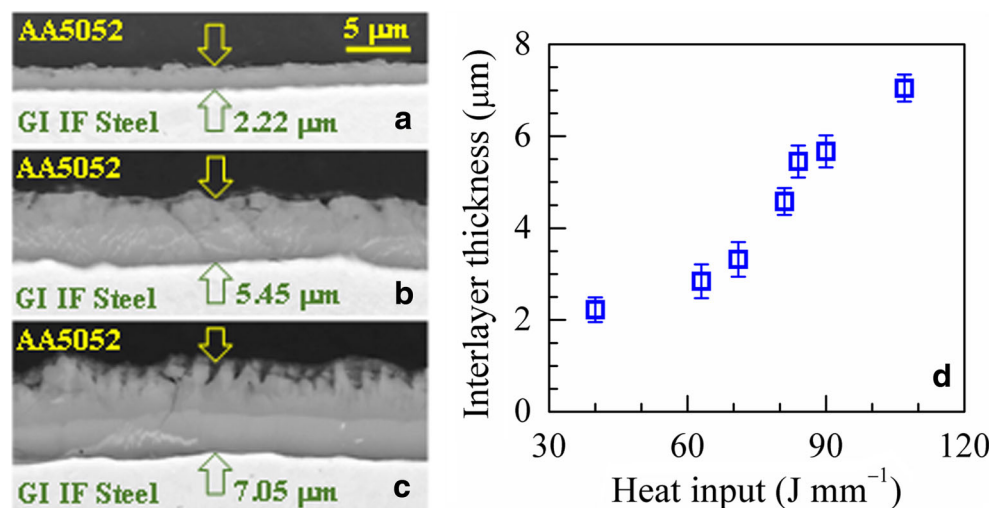
3.3 Effect of heat input on joint porosity and interfacial layer

Figure 5a–c depicts transverse joint cross sections for the heat inputs of 40 J mm^{-1} , 84 J mm^{-1} , and 107 J mm^{-1} , respectively. A comparison of Fig. 5a–c shows greater pores in the bead deposit made at the lowest heat input that is attributed to faster solidification time at smaller heat inputs [2, 10]. In order to examine the effect of heat input on joint porosity, the average area of pores as a percentage of total deposit area is measured over five random cross sections for each process condition and plotted as function of heat input in Fig. 5d. The average pore areas reduce from 13 to 1% with increase in heat input from 40 J mm^{-1} and 107 J mm^{-1} , that is, attributed to efficient

escape of Zn-vapor from the molten bead deposit as observed in open literature [7, 9].

Figure 6a–c presents the backscattered SEM images of the joint interface for the heat inputs of 40 J mm^{-1} , 84 J mm^{-1} , and 107 J mm^{-1} , respectively. The images show the formation of a consistent interface layer that primarily consist of Fe-Al IMC's as seen from the spot EDS analyses as presented in Fig. 7a, b and also reported by Das et al. [10]. The average thickness of the joint interface layer is measured over ten locations for each process condition and plotted as a function of heat input in Fig. 6d. A steady growth of the joint interface layer from $2.22 \mu\text{m}$ (± 0.19) to $7.05 \mu\text{m}$ (± 0.28) is noted with rise of heat input from 40 J mm^{-1} and 107 J mm^{-1} , that is, attributed to greater diffusion of Fe atoms into the Al matrix of the filler deposit at higher heat inputs [4]. Fig. 7a, b shows the EDS spot analyses at selected joint interface locations for two different heat inputs and indicate the presence of multiple Fe-

Fig. 6 a–c Backscattered SEM images of the interface layer at three different heat inputs (in J mm^{-1}) of **a** 40, **b** 84, and **c** 107. **d** Variation in interface layer thickness as a function of heat input



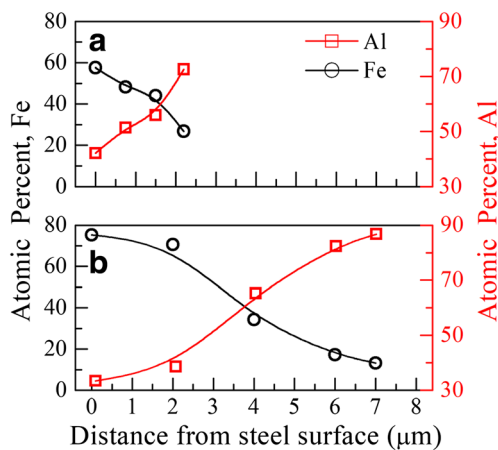


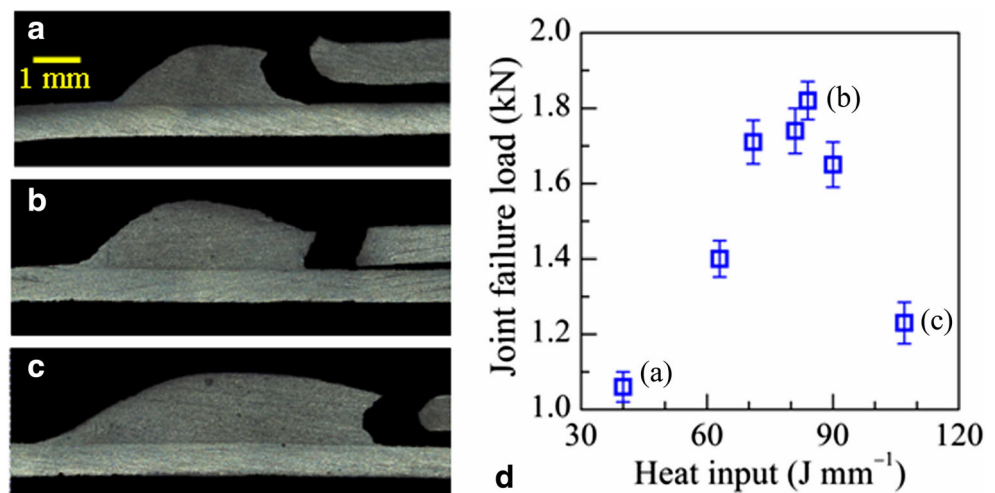
Fig. 7 a, b Spot EDS analyses at selected joint interface locations for two different heat inputs (in J mm^{-1}) of a 40 and b 107

Al intermetallic phases with the elemental Al concentration increasing steadily away from the steel surface.

3.4 Effect of heat input on joint strength

Figure 8a–c shows the images of the fractured specimens on conclusion of the shear-tensile test corresponding to heat inputs of 40 J mm^{-1} , 84 J mm^{-1} , and 107 J mm^{-1} , respectively. Figure 8a indicates the fracture initiation at the root of the bead deposit that has progressed through the deposit (AA4043), which has a lower strength as compared to both AA5052 and steel sheets (Table 2). Increase in heat input has resulted in an apparent shift of the fracture location towards the top aluminum sheet as seen in Fig. 8b, c. This is attributed to a reduction in mechanical strength of the AA5052 alloy, which is used as the top sheet, by almost 15% at elevated temperature [18]. It is noteworthy that failure at the joint interface is not observed for the range of process conditions considered here, which is otherwise reported in literature [10] and often attributed to the interfacial porosities and insufficient wetting of the steel sheets [5, 9]. The pulsed current GMA process with short-circuit metal

Fig. 8 Fractured joint samples at three different heat inputs (in J mm^{-1}) of a 40, b 84, and c 107. d Variation in joint failure load as a function of heat input



transfer used in the current study is successful in providing adequate interface wetting and reducing interfacial pores as evident from Figs. 4 and 6.

Figure 8d presents the variation in peak failure load of the tensile test specimens as a function of heat input for all samples in the range of process conditions considered here. The failure load increases with increase in heat input up to a critical limit followed by a decrease of the joint failure load. The initial increase in failure load with heat input is attributed to decreasing contact angles (θ) that result in lowering of stress concentrations at the toe point. In contrast, excessive increase in heat input renders the work-hardened AA5052 weaker due to possible recrystallization as the material experiences temperatures in excess of 623 K [18]. The maximum joint failure load of 1.82 kN was obtained at a heat input of 84 J mm^{-1} implying 86% joint efficiency considering the failure load of the top aluminum sheet (AA5052) as 2.09 kN at room temperature.

3.5 Effect of heat input on joint distortion

Figure 9 schematically presents the distorted shape of the joint assembly prior to and after the joining process is completed. The thermal distortion of the joined assembly is evaluated along three longitudinal sections A-A, B-B, and C-C (Fig. 9) for each process condition as $\delta = \sqrt{(\delta x^2 + \delta y^2 + \delta z^2)}$, where δx , δy , and δz are the shift of a point respectively in x-, y-, and z-directions due to joining. In particular, the final measurement is made after the joint assembly is cooled to room temperature and the clamps were released. Figure 10a–f presents the measured distortions along the sections A-A, B-B, and C-C for various process conditions. The distortion on the top aluminum sheet is found to be significantly higher than that of the bottom steel sheet, which is attributed to greater coefficient of thermal expansion and lower yield strength of the aluminum alloy. Table 3 also indicates a significant decay in the yield strength of AA5052 as temperature increases beyond 850 K.

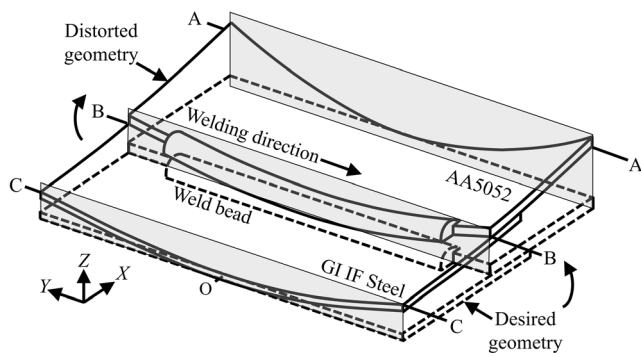


Fig. 9 Schematic presentation of induced thermal distortion in joining of aluminum alloy and galvanized steel sheet

Figure 10a–c shows the measured thermal distortion for a constant wire feed rate of 5.0 m min^{-1} and at three different travel speeds of 5.0 mm s^{-1} , 7.5 mm s^{-1} , and 12.5 mm s^{-1} , respectively. The maximum distortion varies from 9.91 to 5.90 mm as the travel speed is increased from 5.0 to 12.5 mm s^{-1} , that is, attributed to reduced heat input with increase in travel speed. Figure 10d–f depicts the measured distortions at a constant travel speed of 7.5 mm s^{-1} and for three different wire feed rates of 4.5 m min^{-1} , 5.5 m min^{-1} , and 6.0 m min^{-1} , respectively. The maximum distortions in Fig. 10d–f increase from 7.36 to 9.13 mm as the wire feed rate is increased from 4.5 to 6.0 m min^{-1} , that is, attributed to rise in heat input at higher wire feed rates. A comparison of Fig. 10a–f further indicates increase

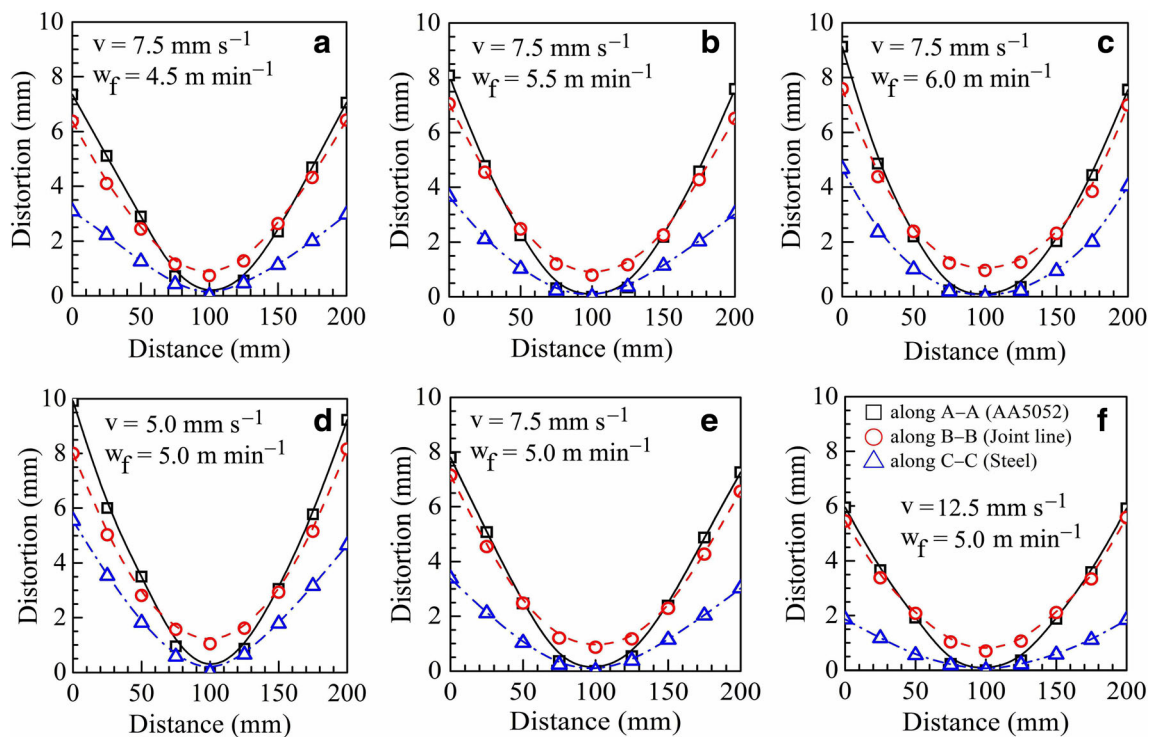


Fig. 10 Measured joint distortions in GMA joined steel-aluminum mixed-metal assembly along three longitudinal sections (A-A, B-B, and C-C as shown in Fig. 1) at three different wire feed rates (w_f) (a, b, c) and at three different travel speeds (v) (d, e, f)

Table 3 Properties of AA5052, AA4043, and GI (IF) steel between 300 and 850 K [19, 20]

Material →	AA5052			AA4043			GI (IF) steel		
Temperature (K) →	300	600	850	300	600	850	300	600	850
Property ↓									
Thermal diffusivity ($10^{-6} \text{ m}^2 \text{ s}^{-1}$)	35	45	42	37	40	41	10	7	4
Coefficient of thermal expansion (10^{-6} K^{-1})	23	27	30	16	21	26	12	14	15
Yield strength (MPa)	90	60	10	70	40	10	160	150	140

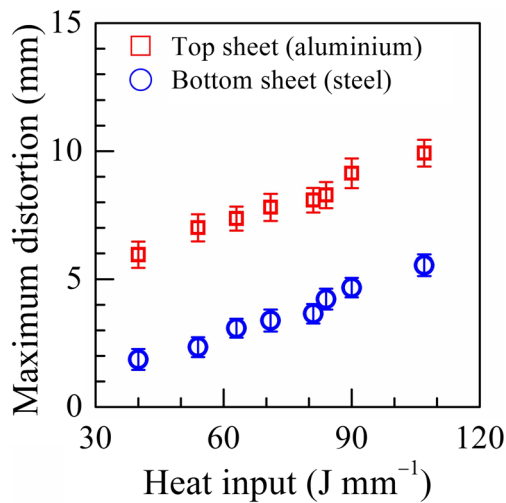


Fig. 11 Measured values of maximum joint distortions as a function of heat input

in thermal distortion by 13% and 5% with unit increase in wire feed rate and decrease in travel speed, respectively. Figure 11 presents the variation of maximum distortions recorded on both the aluminum and steel plates with change in heat input. The maximum distortions are observed to increase linearly with heat input on both the aluminum and steel side with the magnitude of the distortion on the aluminum side far higher than that on the side of the steel sheets.

In summary, an advanced GMA process with fast responsive modulation of current and voltage pulses is used to join aluminum alloy and zinc-coated steel sheets at fairly low heat inputs. Although sound joints are obtained with low to moderate porosity and interface phase layer thicknesses, the mismatch in thermophysical and mechanical properties of the workpiece alloys has resulted in differential thermal distortion, which needs to be addressed further for future commercial success of such applications.

4 Conclusion

Advanced GMA-based joining process can produce sound, defect-free lap joints between 1.0 mm-thick AA5052 and 0.8 mm-thick GI (IF) steel sheets with a 1.0 mm AA4043 filler wire as evaluated in the present work within a selected range of heat input of 40 to 107 J mm⁻¹. The maximum joint efficiency of 86% is achieved corresponding to a heat input of 84 J mm⁻¹ with the failure of the joint in the heat-affected region of AA5052 sheet. The thermal distortion of the joint assembly is found to be of complex nature with the aluminum side exhibiting much higher distortion compared to that in the steel side. The overall heat input during the joining process was found to have a significant impact on the nature and the magnitude of the thermal distortion of the steel-aluminum mixed-metal assembly.

References

1. Thomy C, Vollertsen F (2012) Laser-MIG hybrid welding of aluminium to steel – effect of process parameters on joint properties. *Weld World* 56:124–132
2. Das A, Shome M, Goecke S-F, De A (2017) Joining of aluminium alloy and galvanized steel using a controlled gas metal arc process. *J Manuf Process* 27:179–187
3. Sierra G, Peyre P, Beaume FD, Stuart D, Fras G (2008) Steel to aluminium braze welding by laser process with Al-12Si filler wire. *Sci Technol Weld Join* 13:430–437
4. Zhang HT, Feng JC, He P (2008) Interfacial phenomena of cold metal transfer (CMT) welding of zinc coated steel and wrought aluminum. *Mater Sci Technol* 24:1346–1349
5. Su Y, Hua X, Wu Y (2014) Influence in alloy elements on microstructure and mechanical property of aluminum–steel lap joint made by gas metal arc welding. *J Mater Process Technol* 214: 750–755
6. Cao R, Yu G, Chen JH, Wang PC (2013) Cold metal transfer joining of aluminum alloys-to-galvanized mild steel. *J Mater Process Technol* 213:1753–1763
7. Dong H, Hu W, Duan Y, Wang X, Dong C (2012) Dissimilar metal joining of aluminum alloy to galvanized steel with Al-Si, Al-Cu, Al-Si-Cu and Zn-Al filler wires. *J Mater Process Technol* 212:458–464
8. Yang S, Zhang J, Lian J, Lei Y (2013) Welding of aluminum alloy to zinc coated steel by cold metal transfer. *Mater Design* 49:602–612
9. Yagati KP, Bathe RN, Raajulapati KV, Rao KBS, Padmanabham G (2014) Fluxless arc weld-brazing of aluminium alloy to steel. *J Mater Process Technol* 214:2949–2959
10. Das A, Shome M, Goecke S-F, De A (2015) Joining of galvanized steel and aluminium alloy using controlled short circuiting gas metal arc welding process. *Sci Technol Weld Join* 20(5):402–408
11. Deng D, Murukawa H (2008) Prediction of welding distortion and residual stress in a thin plate butt-welded joint. *Comput Mater Sci* 43:353–365
12. Goecke S-F, Syed AA, Spiegel ME, De A (2013) Probing current, voltage and metal transfer characteristics in pulsed arc and in conventional and a novel low energy input short arc GMAW. *Quart J Jpn Weld Soc* 31(4):26s–30s
13. Frostevarg J, Kaplan AFH, Lamas J (2014) Comparison of CMT with other arc modes for laser-arc hybrid welding of steel. *Weld World* 58:649–660
14. Schenk T, Richardson IM, Kraska M, Ohnimus S (2009) Modeling buckling distortion of DP600 overlap joints due to gas metal arc welding and the influence of the mesh density. *Comput Mater Sci* 46:977–986
15. BS EN 12797:2000 (2004) Brazing – destructive tests of brazed joints. British Standard, London
16. Pepe N, Egerland S, Colegrove PA, Yapp D, Leonhartsberger A, Scotti A (2011) Measuring the process efficiency of controlled gas metal arc welding processes. *Sci Technol Weld Join* 16(5):412–417
17. Makwana P, Shome M, Goecke S-F, De A (2016) Wetting length in gas metal arc brazing of galvanized steel. *Sci Technol Weld Join* 22(2):166–169
18. El-Batahy A, Kutsuna M (2009) Laser beam welding of AA5052, AA5083 and AA6061 aluminium alloys. *Adv Mater Sci Eng* 9. <https://doi.org/10.1155/2009/974182>
19. Gale WF, Totemeier TC (2004) *Smithells metals reference book*, 8th edn. Elsevier, Oxford
20. Mills KC (2002) Recommended values of thermophysical properties for selected commercial alloys. Woodhead, Cambridge